ACS Energy LETTERS

Cite This: ACS Energy Lett. 2018, 3, 713−721

LETTER

Bilateral Interface Engineering toward Efficient 2D−3D Bulk Heterojunction Tin Halide Lead-Free Perovskite Solar Cells

Chenxin Ran,[†,⊥] Jun Xi,[†,§,⊥] Weiyin Gao,[†] Fang Yuan,[†] Ting Lei,[†] Bo Jiao,[†] Xun Hou,[†] and Zhaoxin Wu*[,†,‡]

[†]Key Laboratory for Physical Electronics and Devices of the Ministry of Education & Shaanxi Key Lab of Information Photonic Technique, School of Electronic and Information Engineering, Xi'an Jiaotong University, No. 28, Xianning West Road, Xi'an 710049, China

[‡]Collaborative Innovation Center of Extreme Optics, Shanxi University, Taiyuan 030006, China

[§]Global Frontier Center for Multiscale Energy Systems, Seoul National University, Seoul 08826, Korea

Supporting Information

ABSTRACT: **As a promising substitute for toxic lead-based perovskite, tin (Sn)-based halide perovskite has drawn much attention for photovoltaic applications. However, unsatisfied open-circuit voltage (V_{OC}) and fill factor (FF) values of the available Sn-based perovskite solar cells (PSCs) remain a lingering cloud. In this work, we report a bilateral interfacial engineering strategy to fabricate 2D−3D bulk heterojunction Sn-based perovskite solar cells. Specifically, large cation PEAI and bifunctional LiF are evaporated at the bilateral interfaces of a $FASnI_3$ film. The presence of PEAI improves the V_{OC} and FF of the PSCs via improved surface coverage and the formed 2D−3D bulk heterojunction structure, while the bifunctional LiF (i) lowers the work function of PEDOT:PSS and (ii) facilitates hole extraction at the ITO/PEDOT:PSS interface. This strategy enabled a power conversion efficiency (PCE) of 6.98% with a V_{OC} of 0.47 V and FF of 0.74. Our findings will add critical building bricks toward efficient Sn-based PSCs.**

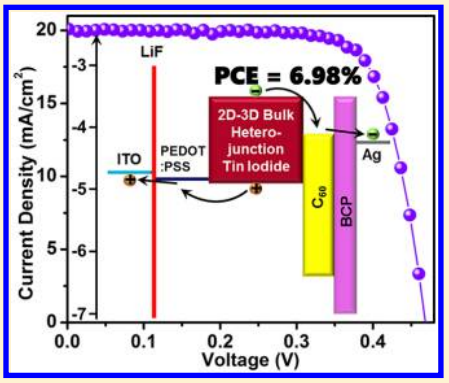

As a rising star in the field of advanced energy materials, organic−inorganic hybrid metal halide perovskite semiconductors have been extensively studied as a "core brain" in many optoelectronic and electronic applications.[1] In particular, solar cell devices based on methylammonium lead triiodide ($MAPbI_3$) perovskite material have proceeded with rapid development, and the latest certificated power conversion efficiency (PCE) of such perovskite solar cell (PSCs) has unprecedentedly achieved 22.1% in small cells and 19.7% in 1 cm^2 cells.[2] Nevertheless, two concerns remain that hamper the large-scale commercial manufacturing of Pb-based PSCs: (i) majority use of the toxic element Pb is fatal to the environment as well as human beings;[3] (ii) there is poor long-term stability of Pb-based perovskite material.[4] With this in mind, great efforts have been made to develop alternative ecofriendly Pb-free perovskite light absorber materials for solar cell application.

To seek eligible Pb substitution, the intrinsic features of the substitution should be considered in the first place. Many of the excellent properties of Pb-based perovskites are considered to originate from the outer $6s^2$ electronic configuration of Pb, which is a configuration of ns^2 that is possessed by many post-transition metal elements.[5] The ns^2 cations in a halide are believed to lead to more delocalized valence and conduction band states by enhancing cation−anion hybridization, from where many superior properties are derived.[6] Theoretically, for photovoltaic application, in addition to the basic optoelectronic properties (suitable band gap, high optical absorption, low carrier effective mass, low exciton binding energy, and high charge mobility), the qualified candidates of efficient and defect-tolerance light absorber material should also possess the properties of a large dielectric constant, small effective masses, a valence band maximum composed of antibonding states, and high levels of band dispersion.[7] In this scenario, post-transition metals with an ns^2 electronic configuration beyond Pb^{2+}, such as Sn^{2+}, Ge^{2+}, Sb^{3+}, and Bi^{3+} cations, possess many of those properties due to their soft polarizability and large spin−orbit effects.[8] In this scenario, they have been of great interest for exploiting efficient nontoxic Pb-free PSCs.[9] Among these Pb-free metal cations, Sn-based perovskite materials are particularly

Received: January 19, 2018
Accepted: February 19, 2018
Published: February 19, 2018

DOI: 10.1021/acsenergylett.8b00085
ACS Energy Lett. 2018, 3, 713−721

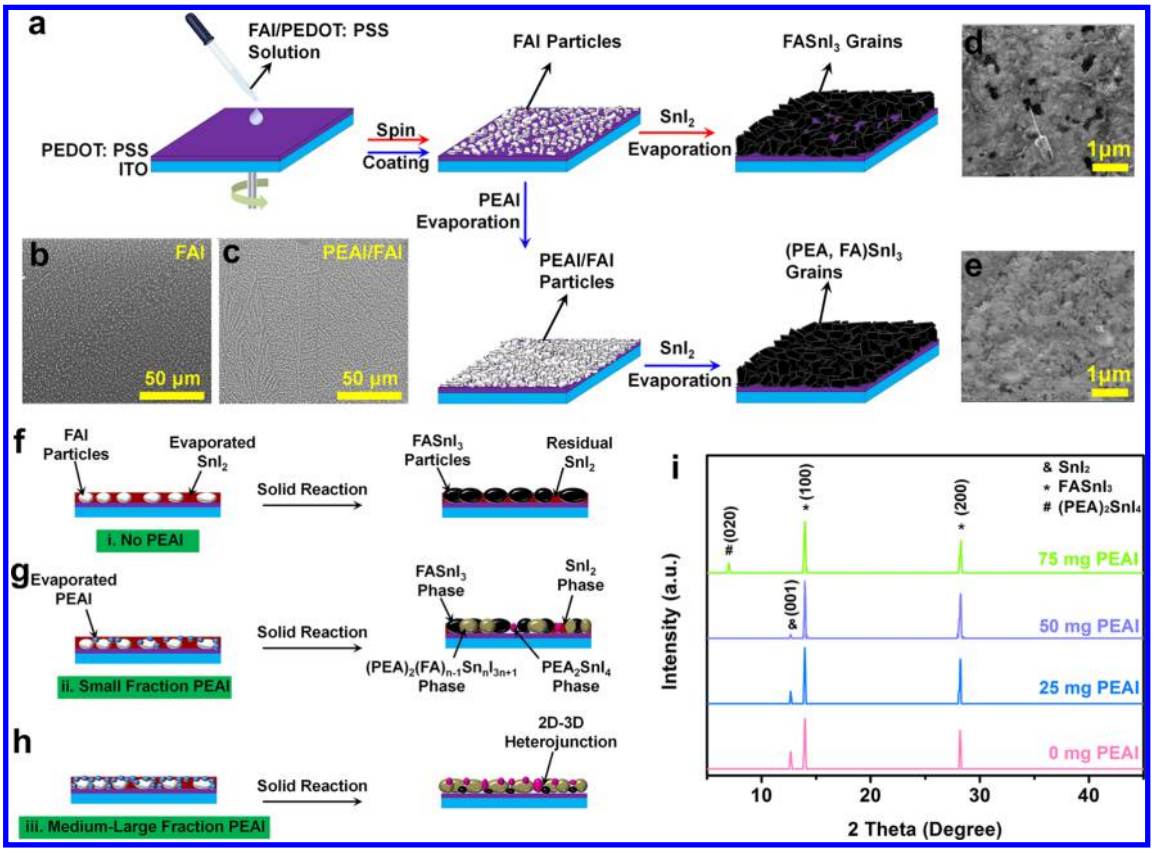

Figure 1. (a) Illustration of the film fabrication strategy with (route in red arrows) and without (route in blue arrows) PEAI evaporation. SEM images of (b) FAI, (c) PEAI, (d) $FASnI_3$, and (e) $(PEA,FA)SnI_3$ films. Illustration of the composition of $(PEA,FA)SnI_3$ films with (f) no PEAI, (g) a small fraction of PEAI, and (h) a medium−large fraction of PEAI. (i) XRD patterns of $(PEA,FA)SnI_3$ films with various evaporated amounts of PEAI.

ideal candidates because both Pb and Sn belong to the same main group (group 14) in the periodic table and possess comparable optical and electrical characteristics. What's more, Sn-based perovskite materials show an absorption edge located in the near-infrared region (900−1000 nm) and are expected to produce higher short-circuit current densities toward higher PCE performance.[10,11] Over the past 3 years, many groups have successfully fabricated Sn-based Pb-free PSCs using both regular and inverted device structures, and considerable progress has been made.[12−25] Among those works, $FASnI_3$-based PSCs have drawn particular attention due to their suitable band gap (1.41 eV) and the single stable phase over a broad temperature range up to 200 °C.[15] The highest reported PCE of $FASnI_3$-based PSCs has reached over 9%.[25] However, the performance (PCE and stability) of the $FASnI_3$-based PSCs is still low due to the following reasons: (i) Sn^{2+} can be easily oxidized into Sn^{4+} owing to the lack of an inert pair effect as in Pb^{2+}, which causes obvious device degradation even under trace amounts of water and oxygen in the glovebox;[13] (ii) the low formation energy of Sn vacancy (V_{Sn}) introduces a deep carrier recombination center, leading to the low fill factor (FF) in PSCs;[15] (iii) the rapid reaction between SnI_2 and FAI salts makes it difficult to control the film morphology fabricated via a one-step spin-coating method; (iv) the mismatch of energy levels between $FASnI_3$ and charge transport layers could set energy barriers at the interfaces and lead to unfavorable charge recombination.

To overcome these problems, researchers have developed a few valid approaches to deposit high-quality $FASnI_3$ film. For example, for the one-step spin-coating film fabrication method, the introduction of SnF_2 additives could efficiently reduce the presence of Sn^{4+} in the film,[15] while DMSO[16] and pyrazine[18] could significantly eliminate the aggregation of SnF_2 on a $FASnI_3$ film. Using diethyl ether as an antisolvent together with SnF_2 additive, Liao et al. achieved a high PCE of 6.22% on an inverted $FASnI_3$ PSC architecture consisting of a PEDOT:PSS hole transport layer (HTM) and C_{60} electron transport layer (ETL).[17] Ke et al. reported that coating mesoporous TiO_2 by a thin ZnS layer to modify the energy level of the interface can enhance performance of the $FASnI_3$ PSCs with a open-circuit voltage (V_{OC}) and PCE of 0.38 V and 5.27%, respectively.[19] Song et al. demonstrated an effective process involving the incorporation of a hydrazine reducing vapor atmosphere to universally deposit Sn-based perovskite films, which can lead to an increased PCE of Sn-based PSCs.[20] Notably, a large ammonium cation, phenylethylammonium (PEA), has been incorporated into FA to form low-dimensional perovskite $PEA_xFA_{(1-x)}SnI_3$ via a one-step antisolvent film fabrication process, where the PCE and stability of the PSCs are efficiently improved due to the passivation effect of a large PEA^+.[25−27] Our group recently developed a novel multichannel interdiffusion two-step film formation protocol to fabricate a $FASnI_3$/PEDOT:PSS hybrid active layer with a promising PCE of 3.98%.[28] However, the relatively low V_{OC} so far of the reported $FASnI_3$-based perovskite solar cells undoubtedly remains the biggest challenge, and more strategies are desired to be developed to further boost the PCE of the PSCs.

DOI: 10.1021/acsenergylett.8b00085
ACS Energy Lett. 2018, 3, 713−721

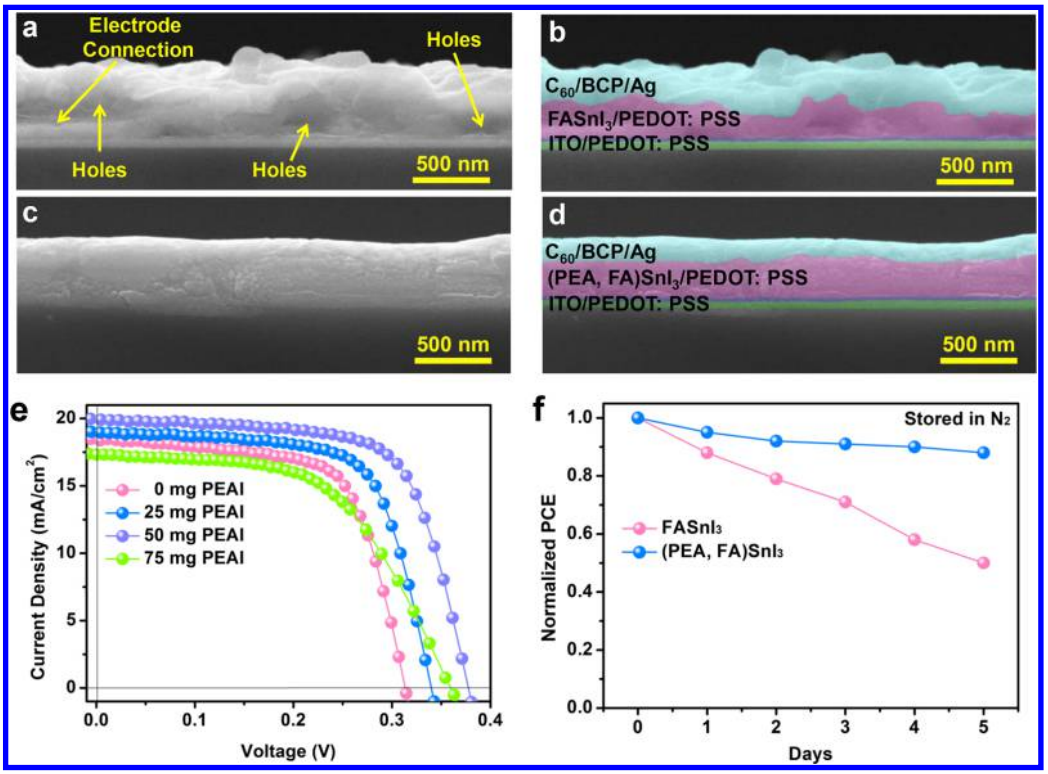

Figure 2. Cross-sectional SEM images of (a,b) $FASnI_3$ and (c,d) $(PEA,FA)SnI_3$ film-based PSCs; (b,d) are colored images of (a,c), respectively. (e) $J-V$ curves of the PSC devices with various evaporated amounts of PEAI and (f) normalized PCE evolution of the device with and without PEAI during 5 days.

In this work, on the basis of the multichannel interdiffusion two-step film fabrication protocol that we developed previously, we improve the PCE of the $FASnI_3$ PSCs (especially V_{OC} and FF) via a bilateral interfacial engineering strategy. Inspired by the works using PEAI to lower the dimensionality and enhance the stability of the perovskite film,[25−27] in this work, the PEAI molecule is first evaporated on top of the FAI film to form a PEAI/FAI mixture. After evaporation of SnI_2, a novel 2D−3D $(PEA,FA)SnI_3$ bulk heterojunction film can be obtained. It was found that this film structure can successfully improve the performance and stability of the PSC device. Sequentially, an ultrathin bifunctional LiF insulating layer, which could (i) lower the work function of PEDOT:PSS and (ii) improve the hole extraction at the ITO/PEDOT:PSS interface, is evaporated at the ITO/PEDOT:PSS interface. This bifunctional LiF layer further improves the V_{OC} and FF of the PSC device. The critical advantage of the bilateral interfacial engineering strategy is that (i) the thermal evaporation of PEAI and SnI_2 under high vacuum could effectively avoid oxidation of the Sn^{2+} and (ii) the use of reductant additive, such as SnF_2 and hydrazine, is able to be debarred. The resulting p−i−n planar heterojunction Pb-free PSCs using the strategy developed here yield a champion efficiency of 6.98%.

We first improve the surface coverage and stability of the $FASnI_3$ film by the introduction of PEAI. As demonstrated in Figure 1a, the original film fabrication process that we developed previously involves the spin-coating of a FAI/PEDOT:PSS aqueous solution (60 mg/mL), evaporation of SnI_2, and postannealing processes to form the $FASnI_3$ film (route with red arrows). The FAI film showed the morphology of well-monodispersed discrete FAI particles (Figures 1b and S1a), which is due to the nucleation of a FAI molecule induced by the active groups on the PEDOT:PSS polymer chains.[28] Although the volume of the FAI molecule would be expanded during the interdiffusion reaction between FAI and SnI_2, the resultant $FASnI_3$ film after SnI_2 evaporation still showed noticeable holes on the film (Figure 1d). It is due to the relatively large spaces between the FAI particles (Figure 1f). In this case, decreasing the spaces between FAI particles can rationally eliminate the holes in the $FASnI_3$ film. One reasonable strategy is to increase the concentration of the FAI/PEDOT:PSS aqueous solution. However, we found that the concentration of FAI in a PEDOT:PSS aqueous solution was unable to further increase because a higher concentration (>60 mg/mL) would lead to sedimentation of the FAI/PEDOT:PSS solvend in aqueous solution, which would result in a nonuniform FAI film after spin-coating and an undulating $FASnI_3$ film surface (Figure S2). To improve the surface coverage of the perovskite film, we ameliorated the film fabrication process by interfacial modification of the FAI film via PEAI evaporation on the top and then evaporation of SnI_2 to form a $(PEA,FA)SnI_3$ bulk heterojunction film (route with blue arrows in Figure 1a). Here, we used the formula $(PEA,FA)SnI_3$ because the $(PEA,FA)SnI_3$ film after introduction of PEAI is composed of multiple phases, as demonstrated in Figure 1g,h. For example, the introduction of a small fraction of PEAI would lead to four possible phases, such as SnI_2, $FASnI_3$, $(PEA)_2(FA)_{n-1}Sn_nI_{3n+1}$, and PEA_2SnI_4 (Figure 1g). The formula $(PEA)_2(FA)_{n-1}Sn_nI_{3n+1}$ represents the mixed FA−PEA Sn perovskite, where n represents the number of tin iodide octahedron layers in the 2D structural unit.[27] In the solution-processed $(PEA)_2(FA)_{n-1}Sn_nI_{3n+1}$ film, n could be readily confirmed by controlling the stoichiometric ratio of every raw material. Because the thermal evaporation technique was used in this study, the evaporated PEAI could be attached both on and between FAI particles. Thus, it is difficult to estimate the

DOI: 10.1021/acsenergylett.8b00085
ACS Energy Lett. 2018, 3, 713−721

precise value of n because the local stoichiometric ratio of PEA and FA is unknown. After further increasing the PEAI amount, medium−large fraction PEAI could yield a 2D−3D bulk heterojunction (PEA,FA)SnI_3 film composed of $FASnI_3$, $(PEA)_2(FA)_{n-1}Sn_nI_{3n+1}$, and PEA_2SnI_4 (Figure 1h) with high surface coverage. It can be observed that both the FAI and $FASnI_3$ films showed higher surface coverage after incorporation of PEAI (Figure 1c,e).

The evolution of the composition change after evaporating various amounts of PEAI was monitored by X-ray diffraction (XRD), as shown in Figure 1i. For the FAI film without PEAI (0 mg of PEAI), the corresponding $FASnI_3$ film showed the typical diffraction peaks at 14.1 and 28.2°, assigned to (001) and (002) planes in orthorhombic patterns of $FASnI_3$ perovskite crystal.[29] Besides, the peak emerging at 12.7° is assigned to the presence of residual SnI_2, which is caused by the spaces between FAI particles (Figure 1f). As the amount of PEAI increases, the diffraction peak of SnI_2 is significantly weakened, which indicates the consumption of excess SnI_2 by the presented PEAI (Figure 1g). Notably, medium−large fraction PEAI (i.e., 75 mg) leads to complete elimination of the SnI_2 diffraction peak, and the emerging diffraction peak at 7.0° is assigned to the (020) facet of a 2D $(PEA)_2SnI_4$ perovskite crystal,[27] which is on account of the reaction between mass PEAI and SnI_2 (Figure 1h). The presence of $(PEA)_2SnI_4$ is further observed in the SEM images of the (PEA,FA)SnI_3 film with 100 mg of PEAI evaporation showing clear plate-like agglomerates (Figure S3). The UV−vis spectra of $FASnI_3$ and (PEA,FA)SnI_3 films are presented in Figure S4a. It can be observed that both films show a typical band-edge located at around 900 nm for 3D $FASnI_3$ structure, where the (PEA,FA)SnI_3 film shows a stronger absorption intensity in the range of 300−700 nm, which is the typical absorption range of lower-dimensional perovskite material, demonstrating the formation of the low-dimensional perovskite phase.[27] Besides, the estimated band gap of the (PEA,FA)SnI_3 film (1.38 eV) is slightly higher than that of the $FASnI_3$ film (1.37 eV) monitored by Tauc plots derived from UV−vis spectra (Figure S4b). The lowered band gap originates from the band gap enlargement effect of the dimensionality reduction of perovskite materials.[30,31] These characterizations of the as-prepared perovskite film demonstrate that the interfacial modification protocol can produce a high-quality 2D−3D hybrid (PEA,FA)SnI_3 bulk heterojunction film.

We fabricated a group of PSC devices with p−i−n configuration to evaluate the photovoltaic performances of the deposited (PEA,FA)SnI_3 film with the device structure of ITO/PEDOT:PSS/(PEA,FA)SnI_3/C_{60}/2,9-dimethyl-4,7-diphenyl-1,10-phenanthroline(BCP)/Ag. The cross-sectional SEM images of the device are shown in Figure 2a−d, where the prominent difference of the devices with and without PEAI evaporation can be observed. For the protocol without PEAI evaporation, the $FASnI_3$ covered by C_{60}/BCP/Ag layers shows the waved cross-sectional topography (Figure 2a,b) with apparent holes and electrode connection, which is in agreement with the surface SEM image (Figure 1d) of the $FASnI_3$ film that shows low surface coverage with noticeable holes. However, for the interfacial modification protocol with PEAI evaporation, the (PEA,FA)SnI_3 device shows much smoother morphology with a film thickness of around 260 nm (Figure 2c,d). Therefore, it is expected that the direct connection between the PEDOT:PSS layer and the C_{60} layer could be largely eliminated and the performance (PCE and stability) of the PSC device could be accordingly enhanced. We have demonstrated that the bulk heterojunction of the perovskite layer incorporated by suitable heterogeneous material could efficiently improve the performance of the PSC device,[32] and the 2D−3D (PEA,FA)SnI_3 bulk heterojunction structure obtained here could be also of great benefit to the PSC device.

Figure 2e shows the typical photocurrent density−voltage (J−V) curves for the planar heterojunction (PHJ) devices prepared with various amounts of PEAI, and the corresponding photovoltaic parameters are summarized in Table 1. The

Table 1. Performance Parameters of $FASnI_3$ PSCs with Different Evaporation Amounts of PEAI[a]

PEAI amount (mg)	V_{OC} (V)	J_{SC} (mA/cm^2)	FF	PCE (%)
0	0.30 ± 0.1	17.25 ± 0.28	0.66 ± 0.02	3.69 ± 0.21
25	0.32 ± 0.2	18.26 ± 0.25	0.67 ± 0.01	4.06 ± 0.19
50	0.37 ± 0.1	19.45 ± 0.20	0.70 ± 0.01	4.89 ± 0.15
75	0.35 ± 0.1	16.68 ± 0.34	0.54 ± 0.02	3.15 ± 0.23

[a]Average and standard deviation values were obtained based on eight cells.

$FASnI_3$ device with 0 mg of PEAI evaporation shows a PCE of 3.85% with a short-circuit current density (J_{sc}) of 18.36 mA/cm^2, an open-circuit voltage (Voc) of 0.31 V, and a fill factor (FF) of 67.6%, which is consistent with our previous work.[28] Surprisingly, upon increasing the amount of evaporated PEAI, the PSC device shows improved J_{SC} and V_{OC}, leading to an improved overall PCE. The highest PCE with an optimized PEAI evaporation amount (50 mg) yielded a champion device showing a PCE of 5.28% with a J_{SC} of 19.96 mA/cm^2, a V_{OC} of 0.38 V, and a FF of 69.6%. However, an excess of PEAI (75 mg) shows decreased photovoltaic performance, though the presence of free SnI_2 is eliminated compared to the trace presence of SnI_2 in a 50 mg PEAI device. On the one hand, it originates from the mass presence of the 2D $(PEA)_2SnI_4$ phase, which is due to its appreciably reduced charge mobility and lower lifetime.[33] On the other hand, this could be explained by the fact that a small amount of SnI_2 phase in the film may play a key role as a defect passivator that could improve the photovoltaic performance of the film.[34] Moreover, the presence of excess Sn halides is reported to be valid in reducing the oxidation of Sn(II) to Sn(IV) due to the reduction effect and the Sn compensation effect.[35] Therefore, a suitable amount of SnI_2 excess could be beneficial to the device performance, which explains the highest performance at 50 mg of PEAI (SnI_2 is still presented as shown in Figure 1i). The stability test of the unencapsulated device stored in a N_2 atmosphere demonstrated the remarkably enhanced stability of a (PEA,FA)SnI_3-based PSC device compared to its counterpart of a pure $FASnI_3$-based device (Figures 2f and S5). In addition, the calculated trap density of the film with PEAI (1.95×10^{15} cm^{-3}) was obviously decreased compared to the film without PEAI (2.97×10^{15} cm^{-3}) (see Figure S6 and Experimental Section for details). It should be ascribed to the enhanced thermodynamic stability of a 2D PEAI-containing perovskite material with efficiently suppressed formation of Sn^{4+}-related defects as identified previously.[26,27] Our recent work has identified that the construction of a dense and smooth Pb-free perovskite film is crucial for a solar cell device to achieve improved V_{OC}, J_{SC}, and PCE.[36] Besides, the introduction of a 2D perovskite into a 3D

DOI: 10.1021/acsenergylett.8b00085
ACS Energy Lett. 2018, 3, 713−721

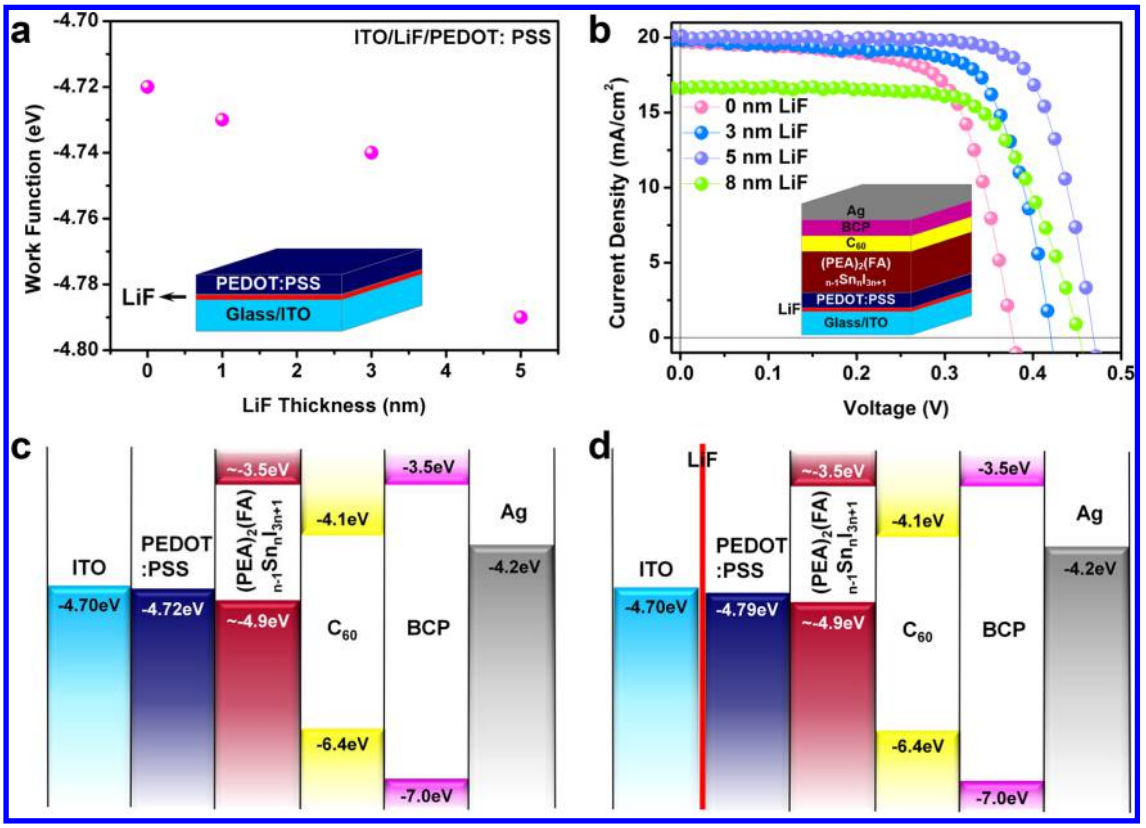

Figure 3. (a) Plots of the work function of a ITO/LiF/PEDOT:PSS film with the function of LiF thickness. (b) *J*−*V* curves of the PSC devices with various thicknesses of the LiF layer; the inset shows the device architecture of the PSCs. Band alignment diagram of the PSC device (c) without and (d) with the ultrathin LiF layer.

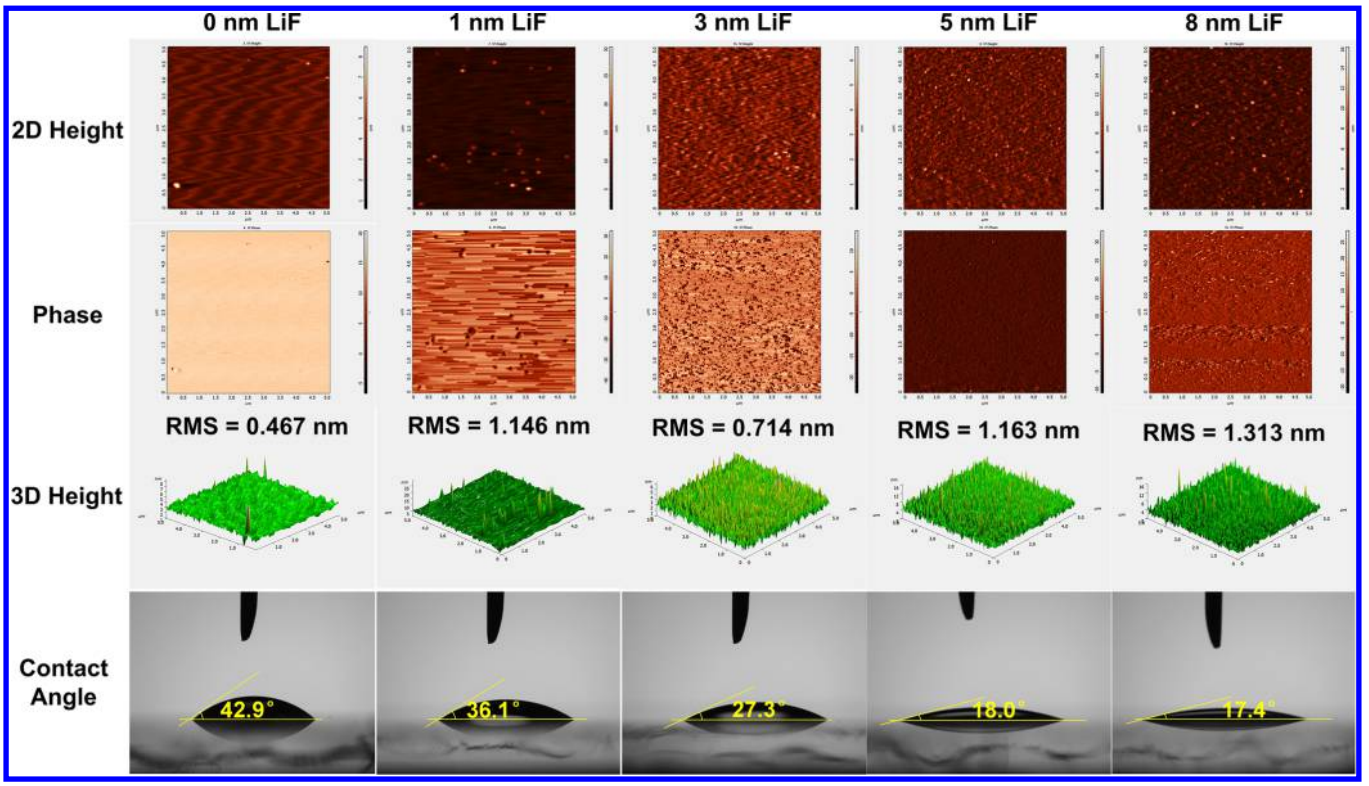

Figure 4. Surface AFM and wettability measurements of LiF films with different evaporation thicknesses on the Si wafer and ITO glass, respectively.

DOI: 10.1021/acsenergylett.8b00085
ACS Energy Lett. 2018, 3, 713−721

perovskite layer to form a hybrid perovskite/perovskite heterojunction has been proved to be valid in reducing the charge recombination rates and stability of the perovskite film.[37] Therefore, the improved surface coverage and the formation of a 2D−3D bulk heterojunction after PEAI introduction rationally improve the performance and stability of the PSCs.

We then attempted to further improve the V_{OC} and FF of the device by interfacial modification at the other side of the perovskite film, that is, the PEDOT:PSS HTL. By inserting an ultrathin layer of LiF between ITO and PEDOT:PSS, we surprisingly found that the work function of the PEDOT:PSS HTL was able to be readily tuned with increasing thickness of the LiF layer. The atmospheric ultraviolet photoelectron spectroscopy measurements (Figure S7) of ITO/LiF/PEDOT:PSS films with various LiF thicknesses show that the work function of PEDOT:PSS deepened from 4.72 down to 4.79 eV as the thickness of LiF increased from 0 to 5 nm (Figure 3a). It should be noted that the work function of PEDOT:PSS obtained in this work (4.72 eV) is very close to that of ITO (4.7 eV) and lower than the reported value (~5.0 eV). It may be attributed to the thin PEDOT:PSS film made from the diluted PEDOT:PSS aqueous solution (PEDOT:PSS/deionized water, v/v = 1/3). To reveal the mechanism of the tunable work function of PEDOT:PSS by the LiF layer, we measured the wettability of the LiF layer with different thicknesses. It is observed that the contact angles of the ITO/LiF substrates gradually decreased as the LiF thickness increased from 0 to 5 nm, while further increasing the LiF thickness to 8 nm resulted in comparable wettability with the 5 nm LiF sample (Figure 4). It has been established that the wettability of a film is largely determined by its surface morphology,[38] and we infer that the wettability variation is attribute to the disparate film morphology of thin LiF (<3 nm). Because ITO on glass is relatively rough, the surface morphology of LiF (1 nm) evaporated on ITO is difficult to distinguish from that of ITO (Figure S8). Alternatively, we verify this conjecture by measuring the surface AFM of the evaporated LiF film on a silicon wafer (with a RMS roughness of 0.467 nm) to give a clear observation of the LiF morphology evolution (Figure 4). It is observed that the morphology of a 1 nm LiF layer shows "isolated island" particles instead of a continuous film, while a 3 nm LiF layer shows the morphology of denser LiF particles but still not a continuous film. A further increase of the thickness of LiF up to 5 nm begins to form a consecutive LiF film consisting of LiF nanoparticles, while 8 nm LiF shows a similar morphology as the 5 nm one. These observations are in agreement with the trend of lowering the contact angle from 0 to 5 nm LiF and the almost unchanged contact angle of 5 and 8 nm LiF (Figure 4). These results suggest that the variation of the wettability of the LiF layers is indeed caused by the different film morphology of evaporated LiF layers with different thickness. The higher wettability of the LiF layer indicates that the PEDOT:PSS aqueous solution can be better spread before spin-coating, which could affect the molecule arrangement of the resultant PEDOT:PSS film. It has been reported that the molecular arrangement of PEDOT:PSS is considered to have an impact on its work function.[39] Therefore, we speculated that the ITO/LiF substrate with various wettability might change the molecular orientation of the spin-coated PEDOT:PSS film, and thus the work function could be accordingly changed.[40] In addition, we found that the evaporated LiF would not be dissolved by PEDOT:PSS solution.

It has been well-established that the maximum V_{OC} of a specific light absorber material in solar cell device is determined by the differentials between the highest occupied molecular orbital (HOMO) of the HTL and the lowest unoccupied molecular orbital (LUMO) of ETL.[41,42] Thus, strategies that lower the HOMO of the HTL material[43−45] and elevate the LUMO of the ETL[46,47] to match the band edges of the light absorber material are proved to be effective for V_{OC} improvement. Therefore, it is expected that the work function tuning of PEDOT:PSS could improve the V_{OC} of the PSCs. We fabricated the solar cell device with an ultrathin evaporated LiF insulating layer, and the device structure can be found in the inset of Figure 3b. The corresponding photovoltaic parameters of the devices with different LiF thicknesses are summarized in Table 2. It can be observed that as the thickness of LiF increased from 0 to 5 nm, the V_{OC} and FF both notably improved. The improvement of V_{OC} from 0.38 to 0.47 V (increased by 0.09 V) agrees well with the lowered work function of PEDOT:PSS (~0.07 eV). The conversion between volts and electronvolts follows the equation $V = E/q$, where E is the energy level in electronvolts and q is the elemental charge. However, the improvement of FF from 67.5 up to 74.0% is attributed to the tunneling effect of an ultrathin LiF insulating layer,[48] which lowers the energy barrier at the ITO/PEDOT:PSS interface. This process allows the collected holes in the PEDOT:PSS HTL to be rapidly extracted by ITO crossing LiF. In this process, the charge recombination at the PEDOT:PSS/perovskite interface can be efficiently suppressed by the presence of the ultrathin insulating layer to achieve a high J_{SC} and FF of the device.[44] Another possibility in addition to tunneling is that the conduction occurs through holes/cracks in the ultrathin LiF, in other words, the area of the PEDOT:PSS/perovskite interface is greatly reduced. This will also suppress recombination at this interface. However, further increase of the thickness of LiF to 8 nm leads to the decreased PCE of the solar cell device, where V_{OC}, J_{SC}, and FF all reduce, which is due to the weakened tunneling effect of the thicker LiF that blocks the efficient hole extraction by ITO.[48] Figure 3c,d illustrates the energy diagram of each layer in the devices with and without the LiF layer. It has been reported that the HOMO of a fresh-made $FASnI_3$ film was ~4.9 eV; thus, the LUMO is estimated to be ~3.5 eV according to the band gap and HOMO values of $FASnI_3$. The much lower HOMO of $FASnI_3$ (~6.0 eV) reported in other literature is owed to the lowering of the ionization energy by the oxidation of Sn^{2+} into Sn^{4+}.[49] The HOMO and LUMO of the evaporated nanothin C_{60} layer is reported to be 6.4 and 4.1 eV,[50] respectively, where the LUMO

Table 2. Performance Parameters of $FASnI_3$ PSCs with Different LiF Thicknesses[a]

LiF thickness (nm)	V_{OC} (V)	J_{SC} (mA/cm^2)	FF	PCE (%)
0	0.37 ± 0.1	19.45 ± 0.20	0.70 ± 0.01	4.89 ± 0.15
3	0.41 ± 0.2	19.58 ± 0.25	0.71 ± 0.02	5.78 ± 0.18
5	0.46 ± 0.1	19.64 ± 0.36	0.72 ± 0.01	6.55 ± 0.22
8	0.44 ± 0.1	16.32 ± 0.34	0.63 ± 0.02	4.52 ± 0.19

[a]Average and standard deviation values were obtained based on 20 cells for 5 nm LiF and 8 cells for others.

DOI: 10.1021/acsenergylett.8b00085
ACS Energy Lett. 2018, 3, 713−721

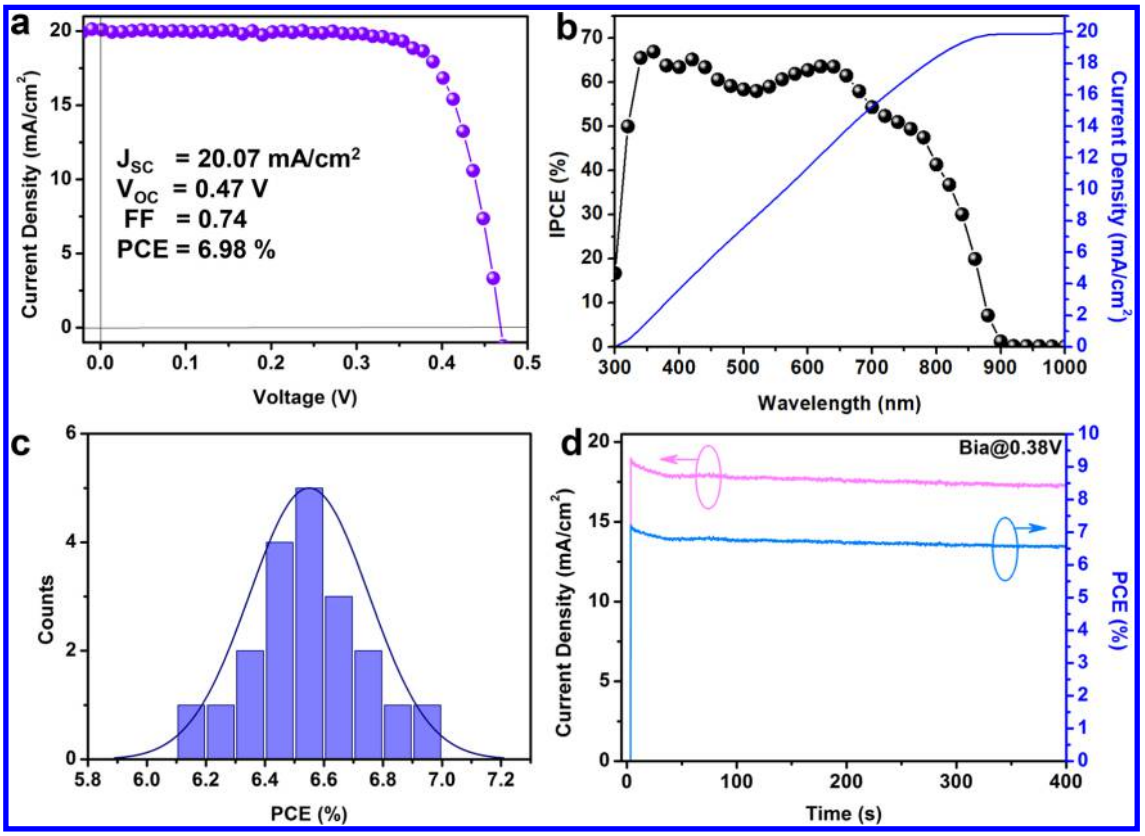

Figure 5. (a) $J-V$ curves and (b) IPCE spectra and integrated J_{SC} for the best-performing device. (c) Statistics of the PCE distribution based on 20 PSC devices. (d) Steady-state photocurrent and output power of the best-performing device over a period of 400 s at a bias of 0.38 V under standard test conditions.

level does not match well with the LUMO level of $FASnI_3$, keeping an open mind for further optimization in ETL material. Through interfacial modification by inserting an ultrathin layer of LiF (Figure 3d), the work function of PEDOT:PSS downshifts from −4.72 to −4.79 eV, and the latter is closer to the HOMO level of the $FASnI_3$ layer. In addition, it has been reported that the introduction of a thin insulating layer is equivalent to reduction of the potential barriers promoting the carriers tunneling through and thus enhances the tunneling current.[48] As a result, the ultrathin LiF layer could favor (i) more matching between the HOMO of PEDOT:PSS and perovskite and (ii) more efficient hole transfer, proving the improved V_{OC} and FF of the PSC devices.

The 2D−3D $(PEA,FA)SnI_3$ bulk heterojunction structure together with a bifunctional LiF layer dramatically boosted the performance of the Sn-based Pb-free PSCs up to 6.98% with a J_{SC} of 20.07 mA/cm^2, V_{OC} of 0.47 V, and FF of 74% (Figure 5a). Negligible hysteresis can be observed in both forward and reverse scan directions (Figure S9). To measure the carrier diffusion property in the efficient PSC device, the PL decay spectra of the $(PEA,FA)SnI_3$ film with and without an interfacial layer are measured, as shown in Figure S10. The carrier lifetimes fitted by a single-exponential function are 0.92, 0.67, and 0.52 ns for bare $(PEA,FA)SnI_3$, $(PEA,FA)SnI_3$/PEDOT:PSS, and $(PEA,FA)SnI_3/C_{60}$, respectively. On the basis of this, the diffusion lengths (L_D) for the electron and hole are calculated to be 205 and 143 nm, respectively (see the Experimental Section for details). The incident photon-to-current efficiency (IPCE) spectra of the device (Figure 5b) show a relatively wide range of photocurrents starting from 900 nm, which is consistent with the band gap of $FASnI_3$ (∼1.4 eV). Besides, the IPCE value in the 300−800 nm range remains high (above 50% with a maximum of 65%), and the integrated J_{SC} value for the IPCE curve agrees well with the high J_{SC} obtained from $J-V$ scanning (∼20 mA/cm^2). The statistics of PCE distribution based on 20 devices shown in Figures 5c and S11 indicates the reliability and repeatability of our film fabrication process. Moreover, the steady-state photocurrent and output power of the best-performing device are measured over a period of 400 s at a bias of 0.38 V under AM 1.5G, 100 mW/cm^2 irradiation (Figure 5d), where a steady photocurrent of ∼17.5 mA/cm^2 and corresponding output power of ∼6.6% can be yielded. These results indicate that bilateral interfacial modification through the thermal evaporation protocol efficiently improves the photovoltaic performance and stability of the Sn-based PSC device. The device shows the highest FF among the state-of-the-art literature based on tin perovskite light absorber (Table S1).

In conclusion, we developed a bilateral interfacial engineering strategy to fabricate efficient Sn-based Pb-free PSCs, showing the most promising PCE of 6.98% with good reproducibility. Specifically, a large ammonium cation, PEA^+, is introduced to produce a 2D−3D hybrid $(PEA,FA)SnI_3$ bulk heterojunction film with higher surface coverage, smoother morphology, and enhanced stability compared to that of a pure $FASnI_3$ film, resulting in the enhanced PCE and stability of PSCs. While a bifunctional ultrathin LiF insulating layer is thereafter cooperated, it is found to be valid in lowering the work function of the PEDOT:PSS HTL layer and in reducing the charge recombination at the ITO/PDOT:PSS interface, leading

DOI: 10.1021/acsenergylett.8b00085
ACS Energy Lett. 2018, 3, 713−721

to solid improved V_{OC} (0.47 V) and FF (0.74) of the PSC device. The strategy developed in this work will provide useful insight into fabricating high-quality Pb-free perovskite films for achieving promising photovoltaic performance. Further breakthrough in Sn-based perovskite solar cells may lie in exploitation of more efficient interfacial layers that lower the interfacial barriers and facilitate the extraction of free carriers.

■ ASSOCIATED CONTENT

Supporting Information

The Supporting Information is available free of charge on the ACS Publications website at DOI: 10.1021/acsenergylett.8b00085.

Experimental section, supporting analysis of SEM, UV–vis, Tauc plots, device stability test, photoemission spectroscopy, AFM, forward and reverse J–V scan, and reproducibility of the device (PDF)

■ AUTHOR INFORMATION

Corresponding Author

*E-mail: zhaoxinwu@mail.xjtu.edu.cn.

ORCID

Zhaoxin Wu: 0000-0003-2979-3051

Author Contributions

⊥C.R. and J.X. equally contributed.

Notes

The authors declare no competing financial interest.

■ ACKNOWLEDGMENTS

This work was financially supported by the National Natural Science Foundation of China (Grant No. 11574248), International Cooperation by Shaanxi (Grant No. 2015KW-008), China Postdoctoral Science Foundation (Grant No. 2017M613137 and No. 2016M590947), National Key R&D Program of China (Grant No. 2016YFB0400702), and the Fundamental Research Funds for the Central Universities (Grant No. xjj2016031). The SEM work was done at the International Center for Dielectric Research (ICDR), Xi'an Jiaotong University, Xi'an, China.

■ REFERENCES

(1) Zhao, Y.; Zhu, K. Organic-Inorganic Hybrid Lead Halide Perovskites for Optoelectronic and Electronic Applications. *Chem. Soc. Rev.* **2016**, *45*, 655–689.

(2) Yang, W. S.; Park, B. W.; Jung, E. H.; Jeon, N. J.; Kim, Y. C.; Lee, D. U.; Shin, S. S.; Seo, J.; Kim, E. K.; Noh, J. H.; et al. Iodide Management in Formamidinium-Lead-Halide-Based Perovskite Layers for Efficient Solar Cells. *Science* **2017**, *356*, 1376–1379.

(3) Babayigit, A.; Ethirajan, A.; Muller, M.; Conings, B. Toxicity of Organometal Halide Perovskite Solar Cells. *Nat. Mater.* **2016**, *15*, 247–251.

(4) Leijtens, T.; Eperon, G. E.; Noel, N. K.; Habisreutinger, S. N.; Petrozza, A.; Snaith, H. J. Stability of Metal Halide Perovskite Solar Cells. *Adv. Energy Mater.* **2015**, *5*, 1500963.

(5) Ganose, A. M.; Savory, C. N.; Scanlon, D. O. Beyond Methylammonium Lead Iodide: Prospects for the Emergent Field of ns^2 Containing Solar Absorbers. *Chem. Commun.* **2017**, *53*, 20–44.

(6) Du, M. H. Efficient Carrier Transport in Halide Perovskites: Theoretical Perspectives. *J. Mater. Chem. A* **2014**, *2*, 9091–9098.

(7) Brandt, R. E.; Stevanović, V.; Ginley, D. S.; Buonassisi, T. Identifying Defect-Tolerant Semiconductors with High Minority-Carrier Lifetimes: Beyond Hybrid Lead Halide Perovskites. *MRS Commun.* **2015**, *5*, 265–275.

(8) Frost, J. M.; Butler, K. T.; Brivio, F.; Hendon, C. H.; van Schilfgaarde, M.; Walsh, A. Atomistic Origins of High-Performance in Hybrid Halide Perovskite Solar Cells. *Nano Lett.* **2014**, *14*, 2584–2590.

(9) Shi, Z.; Guo, J.; Chen, Y.; Li, Q.; Pan, Y.; Zhang, H.; Xia, Y.; Huang, W. Pb-free Organic-Inorganic Hybrid Perovskites for Photovoltaic Applications: Recent Advances and Perspectives. *Adv. Mater.* **2017**, *29*, 1605005.

(10) Stoumpos, C. C.; Malliakas, C. D.; Kanatzidis, M. G. Semiconducting Tin and Lead Iodide Perovskites with Organic Cations: Phase Transitions, High Mobilities, and Near-Infrared Photoluminescent Properties. *Inorg. Chem.* **2013**, *52*, 9019–9038.

(11) Mitzi, D. B.; Feild, C. A.; Schlesinger, Z.; Laibowitz, R. B. Transport, Optical, and Magnetic Properties of the Conducting Halide Perovskite $CH_3NH_3SnI_3$. *J. Solid State Chem.* **1995**, *114*, 159–163.

(12) Hao, F.; Stoumpos, C. C.; Cao, D. H.; Chang, R. P. H.; Kanatzidis, M. G. Pb-free Solid-State Organic-Inorganic Halide Perovskite Solar Cells. *Nat. Photonics* **2014**, *8*, 489–494.

(13) Noel, N. K.; Stranks, S. D.; Abate, A.; Wehrenfennig, C.; Guarnera, S.; Haghighirad, A. A.; Sadhanala, A.; Eperon, G. E.; Pathak, S. K.; Johnston, M. B.; et al. Pb-free Organic-Inorganic Tin Halide Perovskites for Photovoltaic Applications. *Energy Environ. Sci.* **2014**, *7*, 3061–3068.

(14) Kumar, M. H.; Dharani, S.; Leong, W. L.; Boix, P. P.; Prabhakar, R. R.; Baikie, T.; Shi, C.; Ding, H.; Ramesh, R.; Asta, M.; et al. Pb-free Halide Perovskite Solar Cells with High Photocurrents Realized Through Vacancy Modulation. *Adv. Mater.* **2014**, *26*, 7122–7127.

(15) Koh, T. M.; Krishnamoorthy, T.; Yantara, N.; Shi, C.; Leong, W. L.; Boix, P. P.; Grimsdale, A. C.; Mhaisalkar, S. G.; Mathews, N. Formamidinium Tin-Based Perovskite with Low E_g for Photovoltaic Applications. *J. Mater. Chem. A* **2015**, *3*, 14996–15000.

(16) Hao, F.; Stoumpos, C. C.; Guo, P.; Zhou, N.; Marks, T. J.; Chang, R. P.; Kanatzidis, M. G. Solvent-Mediated Crystallization of $CH_3NH_3SnI_3$ Films for Heterojunction Depleted Perovskite Solar Cells. *J. Am. Chem. Soc.* **2015**, *137*, 11445–11452.

(17) Liao, W.; Zhao, D.; Yu, Y.; Grice, C. R.; Wang, C.; Cimaroli, A. J.; Schulz, P.; Meng, W.; Zhu, K.; Xiong, R. G.; et al. Pb-free Inverted Planar Formamidinium Tin Triiodide Perovskite Solar Cells Achieving Power Conversion Efficiencies up to 6.22%. *Adv. Mater.* **2016**, *28*, 9333–9340.

(18) Lee, S. J.; Shin, S. S.; Kim, Y. C.; Kim, D.; Ahn, T. K.; Noh, J. H.; Seo, J.; Seok, S. I. Fabrication of Efficient Formamidinium Tin Iodide Perovskite Solar Cells through SnF_2-Pyrazine Complex. *J. Am. Chem. Soc.* **2016**, *138*, 3974–3977.

(19) Ke, W.; Stoumpos, C. C.; Logsdon, J. L.; Wasielewski, M. R.; Yan, Y.; Fang, G.; Kanatzidis, M. G. TiO_2-ZnS Cascade Electron Transport Layer for Efficient Formamidinium Tin Iodide Perovskite Solar Cells. *J. Am. Chem. Soc.* **2016**, *138*, 14998–15003.

(20) Song, T. B.; Yokoyama, T.; Stoumpos, C. C.; Logsdon, J.; Cao, D. H.; Wasielewski, M. R.; Aramaki, S.; Kanatzidis, M. G. Importance of Reducing Vapor Atmosphere in the Fabrication of Tin-Based Perovskite Solar Cells. *J. Am. Chem. Soc.* **2017**, *139*, 836–842.

(21) Wang, N.; Zhou, Y.; Ju, M. G.; Garces, H. F.; Ding, T.; Pang, S.; Zeng, X. C.; Padture, N. P.; Sun, X. W. Heterojunction-Depleted Pb-free Perovskite Solar Cells with Coarse-Grained B- γ-$CsSnI_3$ Thin Films. *Adv. Energy Mater.* **2016**, *6*, 1601130.

(22) Marshall, K. P.; Walker, M.; Walton, R. I.; Hatton, R. A. Enhanced Stability and Efficiency in Hole-Transport-Layer-Free $CsSnI_3$ Perovskite Photovoltaics. *Nat. Energy* **2016**, *1*, 16178.

(23) Marshall, K. P.; Walton, R. I.; Hatton, R. A. Tin Perovskite/Fullerene Planar Layer Photovoltaics: Improving the Efficiency and Stability of Pb-free Devices. *J. Mater. Chem. A* **2015**, *3*, 11631–11640.

(24) Ke, W.; Stoumpos, C. C.; Zhu, M.; Mao, L.; Spanopoulos, I.; Liu, J.; Kontsevoi, O. Y.; Chen, M.; Sarma, D.; Zhang, Y.; et al. Enhanced Photovoltaic Performance and Stability with a New Type of Hollow 3D Perovskite {en}$FASnI_3$. *Sci. Adv.* **2017**, *3*, e1701293.

(25) Shao, S.; Liu, J.; Portale, G.; Fang, H. H.; Blake, G. R.; ten Brink, G. H.; Koster, L. J. A.; Loi, M. A. Highly Reproducible Sn-Based

DOI: 10.1021/acsenergylett.8b00085
ACS Energy Lett. 2018, 3, 713–721

Hybrid Perovskite Solar Cells with 9% Efficiency. *Adv. Energy Mater.* **2018**, *8*, 1702019.
(26) Smith, I. C.; Hoke, E. T.; Solis-Ibarra, D.; McGehee, M. D.; Karunadasa, H. I. A Layered Hybrid Perovskite Solar-Cell Absorber with Enhanced Moisture Stability. *Angew. Chem., Int. Ed.* **2014**, *53*, 11232−11235.
(27) Liao, Y.; Liu, H.; Zhou, W.; Yang, D.; Shang, Y.; Shi, Z.; Li, B.; Jiang, X.; Zhang, L.; Quan, L. N.; et al. Highly Oriented Low-Dimensional Tin Halide Perovskites with Enhanced Stability and Photovoltaic Performance. *J. Am. Chem. Soc.* **2017**, *139*, 6693−6699.
(28) Xi, J.; Wu, Z.; Jiao, B.; Dong, H.; Ran, C.; Piao, C.; Lei, T.; Song, T. B.; Ke, W.; Yokoyama, T.; et al. Multichannel Interdiffusion Driven $FASnI_3$ Film Formation Using Aqueous Hybrid Salt /Polymer Solutions toward Flexible Pb-free Perovskite Solar Cells. *Adv. Mater.* **2017**, *29*, 1606964.
(29) Dang, Y.; Zhou, Y.; Liu, X.; Ju, D.; Xia, S.; Xia, H.; Tao, X. Formation of Hybrid Perovskite Tin Iodide Single Crystals by Top-Seeded Solution Growth. *Angew. Chem., Int. Ed.* **2016**, *55*, 3447−3450.
(30) Quan, L. N.; Yuan, M.; Comin, R.; Voznyy, O.; Beauregard, E. M.; Hoogland, S.; Buin, A.; Kirmani, A. R.; Zhao, K.; Amassian, A.; et al. Ligand-Stabilized Reduced-Dimensionality Perovskites. *J. Am. Chem. Soc.* **2016**, *138*, 2649−2655.
(31) Cao, D. H.; Stoumpos, C. C.; Farha, O. K.; Hupp, J. T.; Kanatzidis, M. G. 2D Homologous Perovskites as Light-Absorbing Materials for Solar Cell Applications. *J. Am. Chem. Soc.* **2015**, *137*, 7843−7850.
(32) Ran, C.; Chen, Y.; Gao, W.; Wang, M.; Dai, L. One-Dimensional (1D) [6,6]-Phenyl-C-$_{61}$-Butyric Acid Methyl Ester (PCBM) Nanorods as an Efficient Additive for Improving the Efficiency and Stability of Perovskite Solar Cells. *J. Mater. Chem. A* **2016**, *4*, 8566−8572.
(33) Mitzi, D. B.; Medeiros, D. R.; Malenfant, P. R. L. Intercalated Organic-Inorganic Perovskites Stabilized by Fluoroaryl-Aryl Interactions. *Inorg. Chem.* **2002**, *41*, 2134−2145.
(34) Chen, Q.; Zhou, H.; Song, T. B.; Luo, S.; Hong, Z.; Duan, H. S.; Dou, L.; Liu, Y.; Yang, Y. Controllable Self-Induced Passivation of Hybrid Lead Iodide Perovskites Toward High Performance Solar Cells. *Nano Lett.* **2014**, *14*, 4158−4163.
(35) Konstantakou, M.; Stergiopoulos, T. A Critical Review on Tin Halide Perovskite Solar Cells. *J. Mater. Chem. A* **2017**, *5*, 11518−11549.
(36) Ran, C.; Wu, Z.; Xi, J.; Yuan, F.; Dong, H.; Lei, T.; He, X.; Hou, X. Construction of Compact Methylammonium Bismuth Iodide Film Promoting Pb-free Inverted Planar Heterojunction Organohalide Solar Cells with Open-Circuit Voltage over 0.8 V. *J. Phys. Chem. Lett.* **2017**, *8*, 394−400.
(37) Hu, Y.; Schlipf, J.; Wussler, M.; Petrus, M. L.; Jaegermann, W.; Bein, T.; Muller-Buschbaum, P.; Docampo, P. Hybrid Perovskite/Perovskite Heterojunction Solar Cells. *ACS Nano* **2016**, *10*, 5999−6007.
(38) Yong, J.; Chen, F.; Yang, Q.; Huo, J.; Hou, X. Superoleophobic Surfaces. *Chem. Soc. Rev.* **2017**, *46*, 4168−4217.
(39) Nardes, A. M.; Kemerink, M.; de Kok, M. M.; Vinken, E.; Maturova, K.; Janssen, R. A. J. Conductivity, Work Function, and Environmental Stability of PEDOT:PSS Thin Films Treated with Sorbitol. *Org. Electron.* **2008**, *9*, 727−734.
(40) Kahn, A. Fermi Level, Work Function and Vacuum Level. *Mater. Horiz.* **2016**, *3*, 7−10.
(41) Elumalai, N. K.; Uddin, A. Open Circuit Voltage of Organic Solar Cells: an In-Depth Review. *Energy Environ. Sci.* **2016**, *9*, 391−410.
(42) Chueh, C. C.; Li, C. Z.; Jen, A. K. Y. Recent Progress and Perspective in Solution-Processed Interfacial Materials for Efficient and Stable Polymer and Organometal Perovskite Solar Cells. *Energy Environ. Sci.* **2015**, *8*, 1160−1189.
(43) Schulz, P.; Edri, E.; Kirmayer, S.; Hodes, G.; Cahen, D.; Kahn, A. Interface Energetics in Organo-Metal Halide Perovskite-Based Photovoltaic Cells. *Energy Environ. Sci.* **2014**, *7*, 1377−1381.
(44) Hou, Y.; Chen, W.; Baran, D.; Stubhan, T. N.; Luechinger, A.; Hartmeier, B.; Richter, M.; Min, J.; Chen, S.; Quiroz, C. O. R.; et al. Overcoming the Interface Losses in Planar Heterojunction Perovskite-Based Solar Cells. *Adv. Mater.* **2016**, *28*, 5112−5120.
(45) Zuo, C. T.; Ding, L. M. Modified PEDOT Layer Makes a 1.52 V Voc for Perovskite/PCBM Solar Cells. *Adv. Energy Mater.* **2017**, *7*, 1601193.
(46) Wu, C. G.; Chiang, C. H.; Chang, S. H. A Perovskite Cell with a Record-High-Voc of 1.61 V Based on Solvent Annealed $CH_3NH_3PbBr_3$/ICBA Active Layer. *Nanoscale* **2016**, *8*, 4077−4085.
(47) Wolff, C. M.; Zu, F.; Paulke, A.; Toro, L. P.; Koch, N.; Neher, D. Reduced Interface-Mediated Recombination for High Open-Circuit Voltages in $CH_3NH_3PbI_3$ Solar Cells. *Adv. Mater.* **2017**, *29*, 1700159.
(48) Zhao, J. M.; Zhang, S. T.; Wang, X. J.; Zhan, Y. Q.; Wang, X. Z.; Zhong, G. Y.; Wang, Z. J.; Ding, X. M.; Huang, W.; Hou, X. Y. Dual Role of LiF as a Hole-Injection Buffer in Organic Light-Emitting Diodes. *Appl. Phys. Lett.* **2004**, *84*, 2913−2915.
(49) Zhao, Z.; Gu, F.; Li, Y.; Sun, W.; Ye, S.; Rao, H.; Liu, Z.; Bian, Z.; Huang, C. Mixed-Organic-Cation Tin Iodide for Pb-free Perovskite Solar Cells with an Efficiency of 8.12%. *Adv. Sci.* **2017**, *4*, 1700204.
(50) Schulz, P.; Whittaker-Brooks, L. L.; MacLeod, B. A.; Olson, D.; Loo, Y. L.; Kahn, A. Electronic Level Alignment in Inverted Organometal Perovskite Solar Cells. *Adv. Mater. Interfaces* **2015**, *2*, 1400532.

DOI: 10.1021/acsenergylett.8b00085
ACS Energy Lett. 2018, 3, 713−721